

PAPER • OPEN ACCESS


## Continuous time-resolved estimated synthetic 4D-CTs for dose reconstruction of lung tumor treatments at a 0.35 T MR-linac

To cite this article: Moritz Rabe *et al* 2023 *Phys. Med. Biol.* **68** 235008


View the [article online](#) for updates and enhancements.

You may also like

- [Generation of abdominal synthetic CTs from 0.35T MR images using generative adversarial networks for MR-only liver radiotherapy](#)  
Jie Fu, Kamal Singhrao, Minsong Cao et al.
- [Feasibility of MRI-only photon and proton dose calculations for pediatric patients with abdominal tumors](#)  
Filipa Guerreiro, Lauri Koivula, Enrica Seravalli et al.
- [Comparison of the suitability of CBCT- and MR-based synthetic CTs for daily adaptive proton therapy in head and neck patients](#)  
Adrian Thummerer, Bas A de Jong, Paolo Zaffino et al.



**Joining forces:**  
One complete  
QA solution for  
Dosimetry with  
myQA<sup>®</sup>, QUASAR<sup>™</sup>  
and Radcal<sup>®</sup>!



The diagram features a central wireframe head. Surrounding it is a pink ring labeled 'Risk Management'. This is enclosed within a larger circular structure divided into three colored segments: a dark blue segment labeled 'Machine QA', a green segment labeled 'Patient Specific QA', and a light blue segment labeled 'Medical Imaging QA'.



## PAPER

## OPEN ACCESS

RECEIVED  
10 May 2023REVISED  
22 August 2023ACCEPTED FOR PUBLICATION  
5 September 2023PUBLISHED  
28 November 2023

Original content from this work may be used under the terms of the [Creative Commons Attribution 4.0 licence](#).

Any further distribution of this work must maintain attribution to the author(s) and the title of the work, journal citation and DOI.



# Continuous time-resolved estimated synthetic 4D-CTs for dose reconstruction of lung tumor treatments at a 0.35 T MR-linac

Moritz Rabe<sup>1</sup>, Chiara Paganelli<sup>2</sup>, Henning Schmitz<sup>1</sup>, Giorgia Meschini<sup>2</sup>, Marco Riboldi<sup>3</sup>, Jan Hofmaier<sup>1</sup>, Lukas Nierer-Kohlhase<sup>1</sup>, Julien Dinkel<sup>4,5</sup>, Michael Reiner<sup>1</sup>, Katia Parodi<sup>3</sup>, Claus Belka<sup>1,6,7</sup>, Guillaume Landry<sup>1</sup>, Christopher Kurz<sup>1,9</sup> and Florian Kamp<sup>1,8,9</sup>

<sup>1</sup> Department of Radiation Oncology, LMU University Hospital, LMU Munich, Munich, Germany

<sup>2</sup> Dipartimento di Elettronica, Informazione e Bioingegneria, Politecnico di Milano, Milano, Italy

<sup>3</sup> Department of Medical Physics, Ludwig-Maximilians-Universität München (LMU Munich), Garching (Munich), Germany

<sup>4</sup> Department of Radiology, LMU University Hospital, LMU Munich, Munich, Germany

<sup>5</sup> Comprehensive Pneumology Center, German Center for Lung Research (DZL), Munich, Germany

<sup>6</sup> German Cancer Consortium (DKTK), partner site Munich, a partnership between DKFZ and LMU University Hospital Munich, Germany

<sup>7</sup> Bavarian Cancer Research Center (BZKF), Munich, Germany

<sup>8</sup> Department of Radiation Oncology, University Hospital Cologne, Cologne, Germany

<sup>9</sup> Both authors share last authorship.

E-mail: [moritz.rabe@med.uni-muenchen.de](mailto:moritz.rabe@med.uni-muenchen.de)

**Keywords:** synthetic 4D-CT, MR-linac, propagation method, lung cancer, porcine lung phantom, dose reconstruction

## Abstract

**Objective.** To experimentally validate a method to create continuous time-resolved estimated synthetic 4D-computed tomography datasets (tresCTs) based on orthogonal cine MRI data for lung cancer treatments at a magnetic resonance imaging (MRI) guided linear accelerator (MR-linac). **Approach.** A breathing porcine lung phantom was scanned at a CT scanner and 0.35 T MR-linac. Orthogonal cine MRI series (sagittal/coronal orientation) at 7.3 Hz, intersecting tumor-mimicking gelatin nodules, were deformably registered to mid-exhale 3D-CT and 3D-MRI datasets. The time-resolved deformation vector fields were extrapolated to 3D and applied to a reference synthetic 3D-CT image ( $sCT_{ref}$ ), while accounting for breathing phase-dependent lung density variations, to create 82 s long tresCTs at 3.65 Hz. Ten tresCTs were created for ten tracked nodules with different motion patterns in two lungs. For each dataset, a treatment plan was created on the mid-exhale phase of a measured ground truth (GT) respiratory-correlated 4D-CT dataset with the tracked nodule as gross tumor volume (GTV). Each plan was recalculated on the GT 4D-CT, randomly sampled tresCT, and static  $sCT_{ref}$  images. Dose distributions for corresponding breathing phases were compared in gamma (2%/2 mm) and dose-volume histogram (DVH) parameter analyses. **Main results.** The mean gamma pass rate between all tresCT and GT 4D-CT dose distributions was 98.6%. The mean absolute relative deviations of the tresCT with respect to GT DVH parameters were 1.9%, 1.0%, and 1.4% for the GTV  $D_{98\%}$ ,  $D_{50\%}$ , and  $D_{2\%}$ , respectively, 1.0% for the remaining nodules  $D_{50\%}$ , and 1.5% for the lung  $V_{20Gy}$ . The gamma pass rate for the tresCTs was significantly larger ( $p < 0.01$ ), and the GTV  $D_{50\%}$  deviations with respect to the GT were significantly smaller ( $p < 0.01$ ) than for the  $sCT_{ref}$ . **Significance.** The results suggest that tresCTs could be valuable for time-resolved reconstruction and intrafractional accumulation of the dose to the GTV for lung cancer patients treated at MR-linacs in the future.

## 1. Introduction

Stereotactic magnetic resonance imaging-guided radiotherapy (MRgRT) of peripheral and central lung tumors has been clinically implemented at MR-guided linear accelerators (MR-linacs) over the last decade. First clinical reports show that high ablative doses can safely be delivered to lung tumors with low rates of high-grade toxicity,

even to challenging entities such as central or ultracentral lung tumors (Finazzi *et al* 2019, Henke *et al* 2019, Regnery *et al* 2022, 2023) in few (3–12) fractions (Finazzi *et al* 2020a, 2020b, Crockett *et al* 2021) or even just a single fraction (Finazzi *et al* 2020c, Palacios *et al* 2022).

Online treatment plan adaptation before each treatment fraction based on the daily patient anatomy can improve target coverage and organ-at-risk (OAR) sparing for MRgRT of lung cancer (Finazzi *et al* 2019, Nierer *et al* 2022). In clinical practice at MR-linacs today, the goal of online plan adaptation is to restore the original treatment plan quality in terms of planned target coverage and OAR sparing in presence of interfractional changes, without explicit consideration of the accumulated dose that has been delivered in the previous treatment fractions (Finazzi *et al* 2019, Klüter 2019). Interfractional dose accumulation based on fractional magnetic resonance imaging (MRI) datasets and daily delivered dose distributions at MR-linacs is being investigated for a more accurate assessment of the actually delivered dose in research studies for different treatment sites, including the liver (Wahlstedt *et al* 2023) and lung (Rabe *et al* 2023).

For an even more accurate reconstruction of the delivered dose, the effects of intrafractional changes including respiratory-induced tumor and OAR motion must be considered. This is of particular importance for ultra-hypofractionated treatment regimes (Finazzi *et al* 2020b) or single fraction treatments (Finazzi *et al* 2020c, Palacios *et al* 2022) for which dose inhomogeneities do not average out over the course of treatment. Recently, Xiong *et al* (2022) and Wahlstedt *et al* (2022) derived first-order approximations of the intrafractionally accumulated dose delivered in online adaptive MRgRT to the prostate and close-by OARs in presence of residual target motion within a gating window. They neglected interplay effects and assumed the shift-invariance of dose distributions (McCarter and Beckham 2000, Sharma *et al* 2012) in photon therapy and convolved a static dose distribution with the target trajectories observed on planar sagittal cine MR images acquired at MRIdian MR-linacs (ViewRay Inc., Oakwood Village, Ohio, USA). These approximations might be justified for treatment sites with homogeneous tissue densities and small and slow target motion like in the pelvic region. However, larger discrepancies to the actually delivered dose are to be expected when this dose reconstruction method is applied to heterogeneous treatment sites affected by more complex and irregular motion patterns and potentially larger out-of-plane motion (in left-right direction) like lung tumors.

More accurate intrafractional dose accumulation based on real-time MRI requires time-resolved synthetic 4D-computed tomography (CT) data and linac log files (Paganelli *et al* 2018a, Johnstone *et al* 2018, Menten *et al* 2020), which are both currently not available at clinical MR-linacs. In the future, the treatment plan could be updated after each fraction for the remaining fractions, while considering the inter- and intrafractionally accumulated dose that was already delivered to the target and OARs. Ultimately, with fast time-resolved synthetic 4D-CT generation methods, dose calculation, and optimization algorithms, the partially delivered dose could be reconstructed and accumulated in real-time during the treatment fraction itself, and the treatment plan could be continuously adapted based on this information (Kontaxis *et al* 2015, Menten *et al* 2017). Further applications of such time-resolved synthetic 4D-CTs include gating window optimization (Oh *et al* 2019), 4D and robust treatment plan optimization and analysis (Heath *et al* 2009, Meschini *et al* 2022), and the investigation of interplay effects (Rao *et al* 2012, von Münchow *et al* 2022). Furthermore, the dose reconstructed over the whole treatment course could serve as input for clinical dose-response modeling in the post-treatment phase (van Herk *et al* 2018).

Several research groups have developed methods to create time-resolved or respiratory-correlated synthetic 4D-CT datasets for the thoracic or abdominal region based on 3D-CT and time-resolved or respiratory-correlated 4D-MRI data. The common approach is to first deformably register a 3D-CT image to one 3D-MRI dataset of a 4D-MRI dataset to create a synthetic 3D-CT image. Then, the deformation vector fields (DVF) of deformable image registrations (DIRs) between the different breathing phases or time steps of the 4D-MRI dataset are applied to the deformed synthetic 3D-CT image to output a synthetic 4D-CT dataset. However, some methods rely on real-time 4D-MRI sequences (Marx *et al* 2014, Yang *et al* 2015, Grimbergen *et al* 2023) that are not clinically available at MR-linacs and typically provide low spatial resolution. Other methods use a respiratory-correlated 4D-MRI as input data instead (Boye *et al* 2013, Freedman *et al* 2019, Paganelli *et al* 2019, Meschini *et al* 2020), which is time-consuming to acquire and only represents one average breathing cycle that cannot model the intercycle breathing variations that occur during lung cancer treatments (McClelland *et al* 2013). Finally, one method relies on a pre-trained motion model (Müller *et al* 2018), which also uses a respiratory-correlated 4D-MRI as input data and additionally requires pre-treatment model training. Thus, neither of the proposed methods can be currently applied during beam delivery at MR-linacs.

To address these current limitations, we propose a method to create continuous time-resolved estimated synthetic 4D-CTs (tresCTs) at a clinical MR-linac. The method is based on the propagation method, originally proposed for MRI by Paganelli *et al* (2018b). It uses orthogonal cine MRI data, with sagittal and coronal slices intersecting the moving tumor, as input data to deform a reference 3D-MRI dataset to create a continuous time-resolved 4D-MRI dataset. The propagation method yielded the highest tumor tracking accuracy in an *in silico* comparison with similar estimated 4D-MRI generation methods (Paganelli *et al* 2019). Furthermore, the

propagation method to create estimated 4D-MRI datasets has been adapted for use at a MRIdian MR-linac by Rabe *et al* (2021) and experimentally validated with a porcine lung phantom, which showed that the 3D anatomy in the whole phantom thorax could be estimated with high accuracy. Recently, the method has been extended by Meschini *et al* (2022) to create time-resolved virtual CTs based on a 3D-CT dataset and orthogonal cine MRI data acquired at a 3.0 T diagnostic scanner for offline treatment robustness evaluation in carbon-ion radiotherapy of pancreatic cancer.

In this study, we investigated the applicability of the propagation method to generate tresCTs permitting dose calculation for lung cancer treatments at a clinical MR-linac. We propose and describe the continuous tresCT generation method for application during MRgRT for dose reconstruction and report the results of experimental validation measurements with a porcine lung phantom at a CT scanner and MRIdian MR-linac. The geometric and dose calculation accuracy of the tresCTs was determined by comparing the tresCT datasets to acquired ground truth (GT) respiratory-correlated 4D-CT datasets exploiting the reproducibility of the breathing phantom.

## 2. Material and methods

### 2.1. Experimental setup

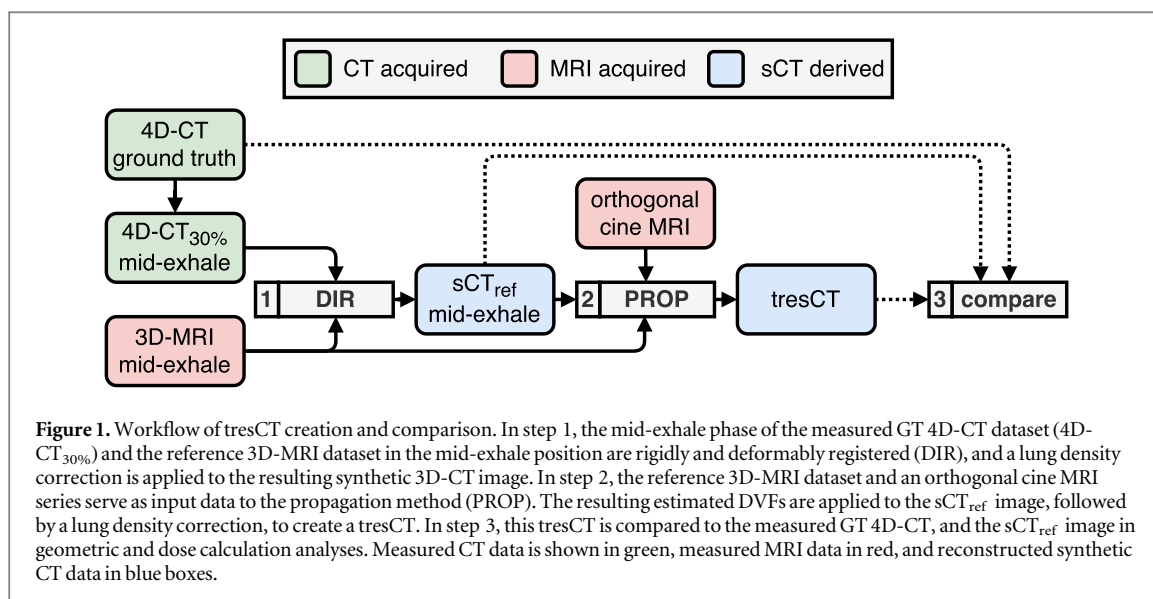
The MR-compatible porcine lung phantom artiCHEST (PROdesign GmbH, Heiligkreuzsteinach, Germany) (Biederer and Heller 2003) was used for the experiments in this study. This phantom mimics patient breathing with an *ex vivo* porcine lung and has been used in a previous experimental validation study to evaluate the geometric accuracy of estimated 4D-MRI datasets created with the propagation method (Rabe *et al* 2021). The phantom and the lung preparation procedure is described in detail in Rabe *et al* (2021) and Rabe (2022). The main components of the phantom are two double-walled shells filled with water that surround an *ex vivo* porcine lung, a water-filled silicone diaphragm located inferiorly to the lung, tubes and hoses connecting the phantom with vacuum and pressure pumps, and a motion control system. *Ex vivo* porcine lungs can be periodically and reproducibly moved by applying air pressure to a silicone membrane at the inferior end of the diaphragm.

The measurements described below were repeated with different motion patterns for two lungs to create three datasets in total (one dataset for lung 1 and two datasets for lung 2). A heated gelatin-water mixture ( $0.3 \text{ g ml}^{-1}$ ) was injected into each lung at various locations. Upon contact with the lung tissue, the mixture solidified and formed four (dataset 1, lung 1) or three (datasets 2 and 3, lung 2) structures. These nodules (ten nodules in total for all datasets) served as surrogate target lesions and OARs. Several nodules were injected per lung to test the tresCT method for different positions within the lung. Periodic motion patterns with a breathing frequency of  $12 \text{ cycles min}^{-1}$ , varying motion amplitudes, and different baseline pressures (determining the maximum lung inflation state) were set at the control system for the three datasets.

The porcine lung phantom was first scanned with a CT scanner, then transported to, and scanned at an MR-linac (datasets 1 and 2). For dataset 3, the phantom was first scanned at the MR-linac before CT imaging. The breathing motion was paused at the inhale position before transport between the two scanners, and the lung position was marked on the upper phantom shell. The experimental setup was connected to an uninterruptible power supply during transport to constantly evacuate the phantom cavity with the vacuum pumps to ensure a stable lung inflation state. The lung position was checked with the marker positions after transport to identify potential deviations between the lung inflation states at the two scanners.

### 2.2. CT data acquisition

The breathing phantom was imaged with a Toshiba Aquilion LB (Canon Medical Systems, Ōtawara, Japan) CT scanner, used in clinical routine for the acquisition of planning CT images for radiotherapy treatment planning. While the phantom was breathing, the projection data for a respiratory-correlated 4D-CT dataset were acquired. Simultaneous to the image acquisition, a surrogate signal correlated to the breathing phase was recorded with a load cell. The load cell is a component of an abdominal pressure belt respiratory gating system (Anzai Medical Co., Ltd, Tokyo, Japan) and was connected to the pressure hose ventilating the diaphragm with a dedicated adapter. The projections were retrospectively assigned to ten breathing phase bins using the vendor's phase-based sorting algorithm to reconstruct a respiratory-correlated 4D-CT dataset (in-plane resolution:  $1.074 \times 1.074 \text{ mm}^2$ ; slice thickness: 3 mm; acquisition matrix:  $512 \times 512$ ; x-ray tube voltage: 120 kV) with ten breathing phases (0%–90% with 10% step size). This respiratory-correlated 4D-CT served as the GT dataset in the geometric and dose calculation analyses described below.



### 2.3. MR-linac data acquisition

The MRI data were acquired at a MRIdian MR-linac using the vendor's torso receiver coils. The treatment delivery system and MRI scanner were decoupled before imaging to operate the MR-linac in quality assurance mode to allow for orthogonal cine MRI acquisition and modification of the sequence parameters.

The following MRI data were acquired: first, the phantom motion was paused at the mid-exhale phase position and a 3D-MRI dataset was acquired with a clinical balanced steady-state free precession (bSSFP) sequence (TrueFISP; sagittal slices; slice thickness: 3 mm; in-plane resolution:  $1.5 \times 1.5 \text{ mm}^2$ ; TR/TE: 3.0/1.27 ms; bandwidth: 604 Hz/pixel; flip angle:  $60^\circ$ ; acquisition matrix:  $360 \times 310 \times 144$ ). This simulated the breath-hold scan typically done clinically. After this scan, the breathing motion was resumed and the phantom was breathing with the same motion pattern as during 4D-CT acquisition. For each injected nodule, one time-resolved orthogonal cine MRI series (TrueFISP; slice thickness: 5 mm; in-plane resolution:  $3.5 \times 3.5 \text{ mm}^2$ ; TR/TE: 2.4/1.1 ms; bandwidth: 1000 Hz/pixel; flip angle:  $60^\circ$ ; acquisition matrix:  $100 \times 100$ ; number of averages: 1) was acquired, where the intersection line of the orthogonal slices was positioned at the approximate nodule centroid position. Each orthogonal cine MRI series consisted of 600 frames (300 in sagittal and 300 in coronal orientation) acquired over a time period of 82 s, corresponding to a frame rate of 7.3 Hz (or 3.65 Hz per sagittal/coronal pair).

### 2.4. Creation of continuous time-resolved estimated synthetic CTs (tresCTs)

For each of the ten gelatin nodules of the three datasets, a tresCT was created following the workflow sketched in figure 1.

For each dataset, all gelatin nodules, the lung, and the diaphragm were delineated on the mid-exhale phase (30%) image of the GT 4D-CT dataset (4D-CT<sub>30%</sub>). The 4D-CT<sub>30%</sub> image was deformably registered to all remaining 4D-CT phase images using regularized B-splines with mean squared error as similarity metric using a multi-stage multi-resolution (4 stages) approach using the software Plastimatch (Shackleford *et al* 2010). The resulting DVFs were applied to the nodule structures defined on the 4D-CT<sub>30%</sub> image to obtain the GT nodule positions in each of the ten breathing phases of the GT 4D-CT.

The 4D-CT<sub>30%</sub> image was then rigidly registered to the mid-exhale phase 3D-MRI dataset using a research version of the treatment planning system RayStation (RaySearch Laboratories, Stockholm, Sweden; version 10.1.100.0) with mutual information as similarity metric. The final registration results were visually inspected in overlay plots by assessing the alignment of the inner and outer phantom walls and ten multimodality markers (MR PinPoint, Par Scientific A/S, Odense, Denmark) attached to the outer surface of the upper phantom shell. The optimal translation and rotation parameters output by the registration were applied to all GT 4D-CT phase images to get the CT and MRI data in the same frame of reference.

The 4D-CT<sub>30%</sub> image was then deformably registered to the mid-exhale 3D-MRI using B-splines with mutual information as similarity metric and three resolution stages using Plastimatch (step 1 in figure 1) to create a synthetic 3D-CT image in the mid-exhale phase, referred to as the reference synthetic 3D-CT (sCT<sub>ref</sub>). By choosing the mid-exhale phase as the reference image phase, we aimed at sampling the nodule motion in both directions towards the inhale phase, as well as towards the exhale phase, since the lung tumor positions observed during gated treatment at the MRIdian MR-linac are typically normally distributed around the position

observed on the daily setup 3D-MRI scans (i.e. the breathing phase used for gating) (van Sörnsen de Koste *et al* 2018). To account for potential differences in the lung inflation state in the 3D-MRI dataset and the 4D-CT<sub>30%</sub> image, the lung density correction described further below was applied to the resulting sCT<sub>ref</sub> image. The nodule contours were transferred from the 4D-CT<sub>30%</sub> image to the sCT<sub>ref</sub> image by applying the corresponding deformation vector field (DVF) of this DIR to the individual structures.

Subsequently, the propagation method was applied to create one tresCT for each of the ten gelatin nodules of the three datasets. The propagation method is described in detail in Paganelli *et al* (2018b), Rabe *et al* (2021) and Rabe (2022). Thus, only a summary of the main steps is given here.

The mid-exhale 3D-MRI was defined as the reference 3D-MRI image (Rabe *et al* 2021) and was input to the propagation method together with the corresponding sCT<sub>ref</sub> image and the orthogonal cine MRI series (step 2 in figure 1). The first 15 slice pairs of the orthogonal cine MRI series were discarded to avoid frames for which the magnetization vector has not yet reached the steady state (Bieri and Scheffler 2013, Rabe *et al* 2021). For each of the remaining 285 slice pairs, the respective sagittal and coronal slices were extracted from the 3D-MRI reference image and deformably registered to the acquired orthogonal cine MRI slice pair in independent DIRs in 2D using Plastimatch, using B-slides at six resolution stages with gradient magnitude as similarity metric. A binary image of the phantom cavity including the lung and diaphragm was used to mask the DIRs to focus the registration on the lung and to allow for sliding motion between the inner phantom walls and the lung tissue (Rabe *et al* 2021). The resulting DVFs were extrapolated to 3D and superimposed using the position-dependent weighting factors depending on the normal distances to the orthogonal slices introduced by Rabe *et al* (2021) (see equations (1)–(4) in their publication). All deformation vectors outside of the lung and diaphragm structures defined on the sCT<sub>ref</sub> image were set to zero to prevent distortions of the static phantom shells due to extrapolation effects, since the DIRs were masked and focused on the lung and diaphragm. The resulting 3D-DVF was applied to the sCT<sub>ref</sub> image to output an estimated synthetic 3D-CT at the respective time point of the acquired orthogonal cine MRI slice pair. Finally, the lung density correction described below was applied to the resulting estimated synthetic 3D-CT. Additionally, the estimated DVFs output by the propagation method were applied to the nodule structures defined on the sCT<sub>ref</sub> to obtain the estimated nodule positions at each time point.

By repeating these steps for all 285 slice pairs (i.e. time points) for each of the ten acquired orthogonal cine MRI series (one for each of the ten gelatin nodules), a total of ten continuous tresCTs with a temporal resolution of 3.65 Hz (half the temporal resolution of the acquired orthogonal cine MRI series, since a pair of a sagittal and a coronal slice is taken as input data) and the voxel size of the GT 4D-CT ( $1.074 \times 1.074 \times 3 \text{ mm}^3$ ) were created.

## 2.5. Lung density correction

To account for lung density changes due to differences in air volume in the breathing states of (a) the 4D-CT<sub>30%</sub> and the reference 3D-MRI dataset (step 1 in figure 1) or (b) the sCT<sub>ref</sub> image and the acquired orthogonal cine MRI slice pairs (step 2 in figure 1), a scaling of the CT numbers of (a) the sCT<sub>ref</sub> image or (b) the tresCT was performed, following the method by Sarrut *et al* (2006) (equation (5) in their publication):

$$HU_1 = \det(\nabla\phi)(1000 + HU_2) - 1000, \quad (1)$$

where  $HU_1$  are the CT numbers in (a) the sCT<sub>ref</sub> image or (b) the tresCT to be corrected,  $HU_2$  are the CT numbers in (a) the 4D-CT<sub>30%</sub> image or (b) the sCT<sub>ref</sub> image, and  $\det(\nabla\phi)$  is the determinant of the Jacobian of the DVF  $\phi$  of (a) the DIR of the 4D-CT<sub>30%</sub> image to the reference 3D-MRI dataset or (b) of the estimated extrapolated DIR in the propagation method.

## 2.6. Breathing phase assignment of tresCTs

The geometric accuracy of each of the ten tresCTs and their usability for dose reconstruction was evaluated by comparing them to the respective GT 4D-CT images (step 3 in figure 1). The tresCTs were additionally compared to the sCT<sub>ref</sub> image to assess the added value of the tresCTs with respect to the current clinical scenario in which no time-resolved synthetic CT data is available for dose reconstruction.

To enable a breathing phase-specific comparison of the tresCT and GT 4D-CT images, the images at all time points of the tresCT had to be assigned to one of the ten breathing phase bins of the GT 4D-CT. For this purpose, a surrogate signal correlated to the breathing phase was derived by summing all pixels in a binary thresholded region of interest of the sagittal slice image of each acquired orthogonal cine MRI slice pair, which included parts of the moving superior boundary of the silicone diaphragm (Rabe *et al* 2021). The time points with the minimum value of summed pixels corresponded to the inhale phase (0% phase in the GT 4D-CT images). The remaining breathing phases were derived by dividing the time period between two inhale positions into ten equitemporal breathing phases. This way, each 3D-CT image of the tresCTs was assigned to one of the ten breathing phase bins.

The images in corresponding breathing phases of the tresCT and GT 4D-CT were compared in geometric and dose calculation analyses described in the following.

## 2.7. Geometrical analysis

The motion amplitudes of the nodule centroids in the GT 4D-CT dataset were measured from the inhale to the exhale phase. The nodule centroid positions were extracted for all ten breathing phases in the GT 4D-CT (GT nodule centroid positions) and all time steps of the tresCT (estimated nodule centroid positions). The tracking error was defined as the Euclidean distance between the estimated and GT nodule centroid positions. The tracking error was calculated for the nodule intersected by both orthogonal slices for all time points for all ten nodules of the three datasets.

## 2.8. Dose calculation evaluation

The dose calculation evaluation was performed with a research version of the ViewRay MRI-dian treatment planning system (version 5.4.0.97). One treatment plan was created for each of the ten surrogate target lesions for the three datasets. For each treatment plan, the 4D-CT<sub>30%</sub> image was used as the planning image, and the nodule structure intersected by the orthogonal slices was defined as the gross tumor volume (GTV). The planning target volume (PTV) was created by expanding the GTV with an isotropic margin of 5 mm, similar to common clinical practice for stereotactic MR-guided adaptive radiotherapy of lung tumors with the MRI-dian MR-linac (Finazzi et al 2020b). A 6 MV flattening-filter-free step-and-shoot intensity-modulated radiotherapy (IMRT) plan with a planned dose of  $5 \times 11$  Gy, prescribed to the PTV, was optimized while considering the effect of the 0.35 T magnetic field to mimic gated stereotactic treatment plans (Finazzi et al 2020b). A total of 14–16 beams with an angular spacing of  $17.1^\circ$  were set up, where angles for which the beam would enter from the non-nodule-bearing lung side were omitted. The plans were normalized to a 95% prescription dose ( $D_p$ ) coverage of the PTV ( $V_{100\%} \geq 95\%$ ) (Finazzi et al 2020b). Following the recommendations of AAPM Task Group 101 for stereotactic body radiation therapy (Benedict et al 2010), dose calculation was performed on an isotropic 2 mm grid with a Monte Carlo algorithm with statistical uncertainty of 1%.

The final optimized plan was recalculated on all GT 4D-CT phases and ten estimated synthetic CTs, where one image per breathing phase was randomly sampled from the tresCT. One plan for each of the ten nodules was created and was recalculated for all ten breathing phases, yielding 100 dose distributions on both the GT and the estimated synthetic CTs. The treatment plan was additionally recalculated on the sCT<sub>ref</sub> image used as input to the propagation method. As during plan optimization, all treatment plan recalculations were performed on an isotropic 2 mm dose grid with a Monte Carlo algorithm with statistical uncertainty of 1% under consideration of the effect of the magnetic field.

## 2.9. Gamma pass rate analysis

For each of the ten breathing phases, the dose distributions on the GT 4D-CT images were compared to the ones on the randomly sampled tresCT images in the same breathing phase and additionally to the static dose distribution of the sCT<sub>ref</sub> image in global gamma analyses with a (2% of  $D_p/2$  mm) passing criterion for all voxels with a dose level above 10% of  $D_p$  in the GT images.

## 2.10. Dose–volume histogram (DVH) parameter analysis

All structures defined on the 4D-CT<sub>30%</sub> image (GTV, remaining nodules, lung, diaphragm) were rigidly copied to all other GT 4D-CT phase images, the randomly sampled tresCT images, and the sCT<sub>ref</sub> image. The DVH parameters were retrieved for these static structures defined on the GT 30% breathing phase to focus the analyses on the region with the highest dose values. The following DVH parameters were retrieved from all recalculated dose distributions: GTV  $D_{98\%}$ , GTV  $D_{50\%}$ , GTV  $D_{2\%}$ ,  $D_{50\%}$  of the remaining nodules (excluding the GTV) for which the  $D_{50\%}$  value in the planned dose distribution exceeded 11 Gy (20% of  $D_p$ ), and lung  $V_{20Gy}$ . The median absolute differences between the GT DVH parameters in the inhale and exhale phase were computed for all analyzed DVH parameters to quantify their variation within a breathing cycle. The absolute relative deviations in percent between the DVH parameters for the GT 4D-CT dataset with respect to the corresponding DVH parameters for the tresCT dataset in the same breathing phase ( $\Delta_{\text{tresCT}}$ ), and the sCT<sub>ref</sub> image ( $\Delta_{\text{sCT}_{\text{ref}}}$ ) were calculated for all DVH parameters  $D$  listed above:

$$\Delta_{\text{tresCT}} = \left| \frac{D_{\text{tresCT}} - D_{\text{GT}}}{D_{\text{GT}}} \right| \cdot 100\% \quad (2)$$

$$\Delta_{\text{sCT}_{\text{ref}}} = \left| \frac{D_{\text{sCT}_{\text{ref}}} - D_{\text{GT}}}{D_{\text{GT}}} \right| \cdot 100\%. \quad (3)$$

**Table 1.** Geometrical analysis results. The GTV size, motion amplitude  $A_{\text{motion}}$ , and tracking error are listed for each of the ten nodules of the three datasets individually and averaged over all nodules.

Dataset	Lung	Nodule	GTV cc	$A_{\text{motion}}$ mm	Tracking error (mean $\pm 1\sigma$ ) mm
1	1	1	14.9	7.0	1.3 $\pm$ 0.7
		2	14.9	7.6	1.9 $\pm$ 0.6
		3	18.2	4.6	1.3 $\pm$ 0.5
		4	17.0	9.9	2.5 $\pm$ 0.7
2	2	1	11.9	13.0	3.4 $\pm$ 1.0
		2	12.1	6.2	2.4 $\pm$ 1.6
		3	10.0	15.9	3.9 $\pm$ 1.0
3	2	1	11.9	6.8	1.4 $\pm$ 0.6
		2	12.1	2.5	1.9 $\pm$ 0.6
		3	10.0	8.0	1.4 $\pm$ 0.6
Averaged values			13.3	8.2	2.1 $\pm$ 0.8

### 2.11. Statistical analysis

Pairwise comparisons of each of the analyzed DVH parameters were performed between  $\Delta_{\text{tresCT}}$  and  $\Delta_{\text{sCT}_{\text{ref}}}$  for each breathing phase individually, and for all breathing phases combined, with a two-tailed Wilcoxon signed-rank test. Furthermore, the gamma pass rates of the tresCT compared to GT 4D-CT analysis and the gamma pass rates of the sCT<sub>ref</sub> compared to GT 4D-CT analysis were also compared pairwise for each breathing phase separately, and additionally for all breathing phases combined, with a two-tailed Wilcoxon signed-rank test. All tests were performed with Python (version 3.6.5) using the implementation of the Wilcoxon signed rank test in the package scipy (scipy.stats.wilcoxon; version 1.5.4). A  $p$ -value  $< 0.05$  was considered to be statistically significant.

## 3. Results

### 3.1. Geometrical analysis

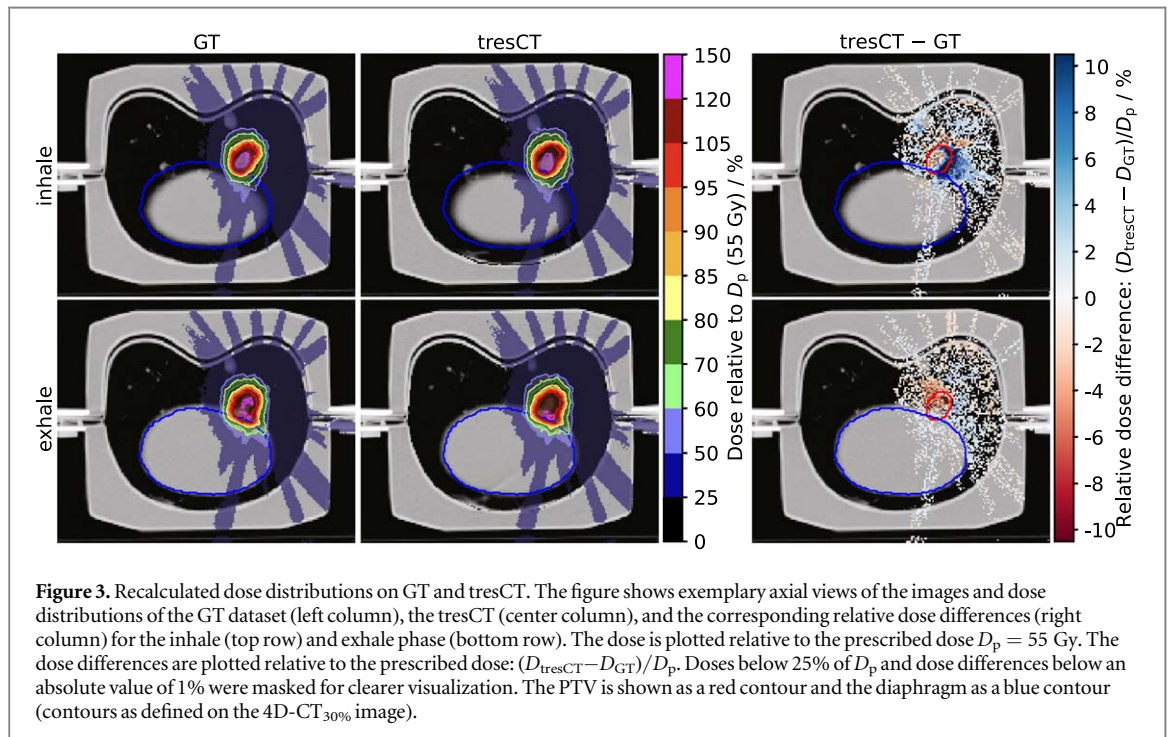
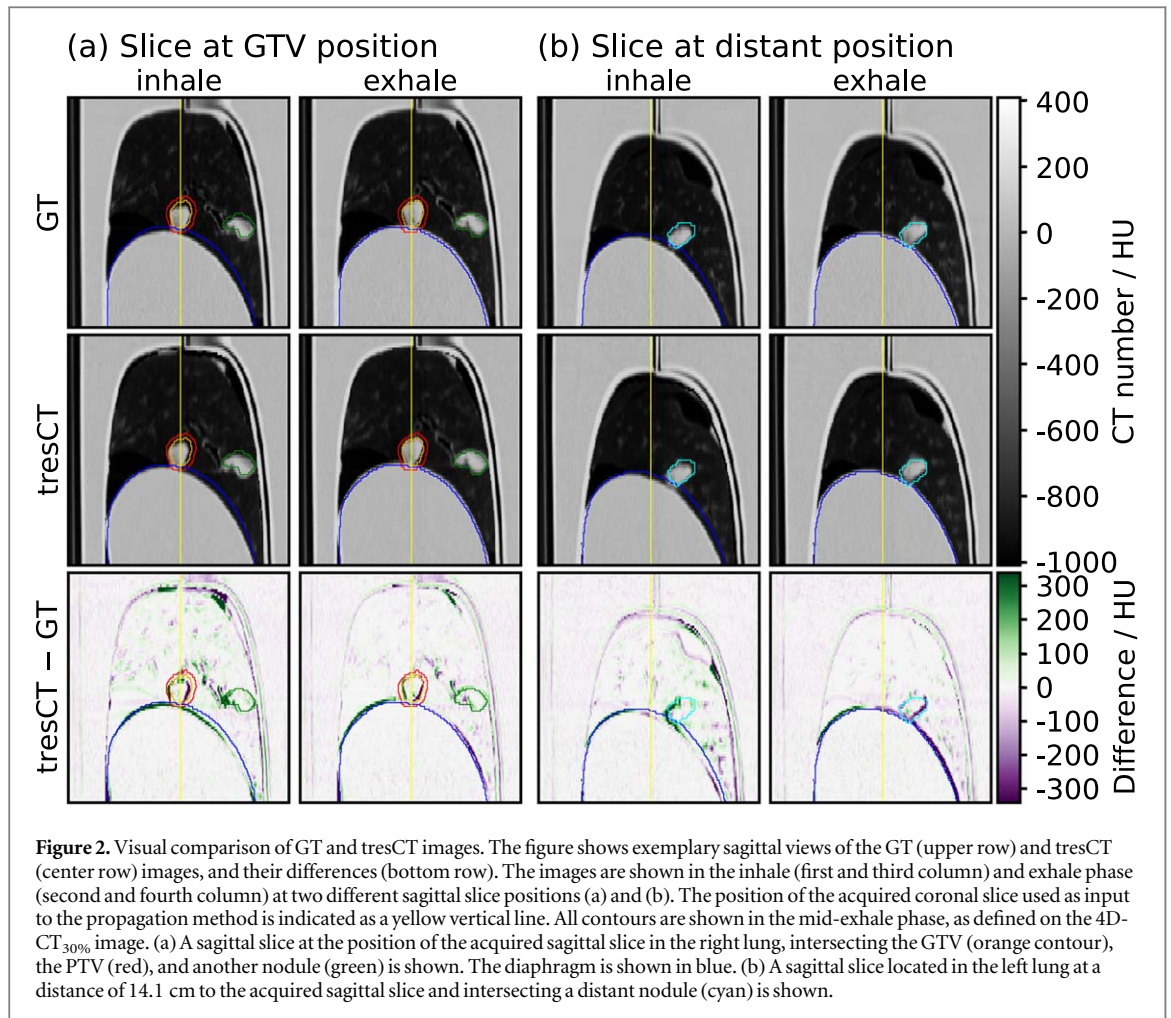
The results of the geometric analysis for each of the ten nodules of the three datasets are listed in table 1. The volumes of the gelatin nodules ranged between 10–18 cc, with a mean value of 13.3 cc. With a breathing frequency of 12 cycles  $\text{min}^{-1}$ , and an acquisition time of 82 s, approximately 16 breathing cycles were recorded during each orthogonal cine MRI series acquisition. The inhale-to-exhale nodule centroid motion amplitudes, measured in the GT 4D-CT datasets, were in the range 3–16 mm, with a mean value of 8.2 mm. The largest mean motion amplitudes were observed for the nodules in dataset 2 (11.7 mm), followed by dataset 1 (7.3 mm), and dataset 3 (5.8 mm). Averaged over all time points and all ten datasets, the (mean  $\pm 1\sigma$ ) tracking error for the nodules intersected by both orthogonal slices was (2.1  $\pm$  0.8) mm.

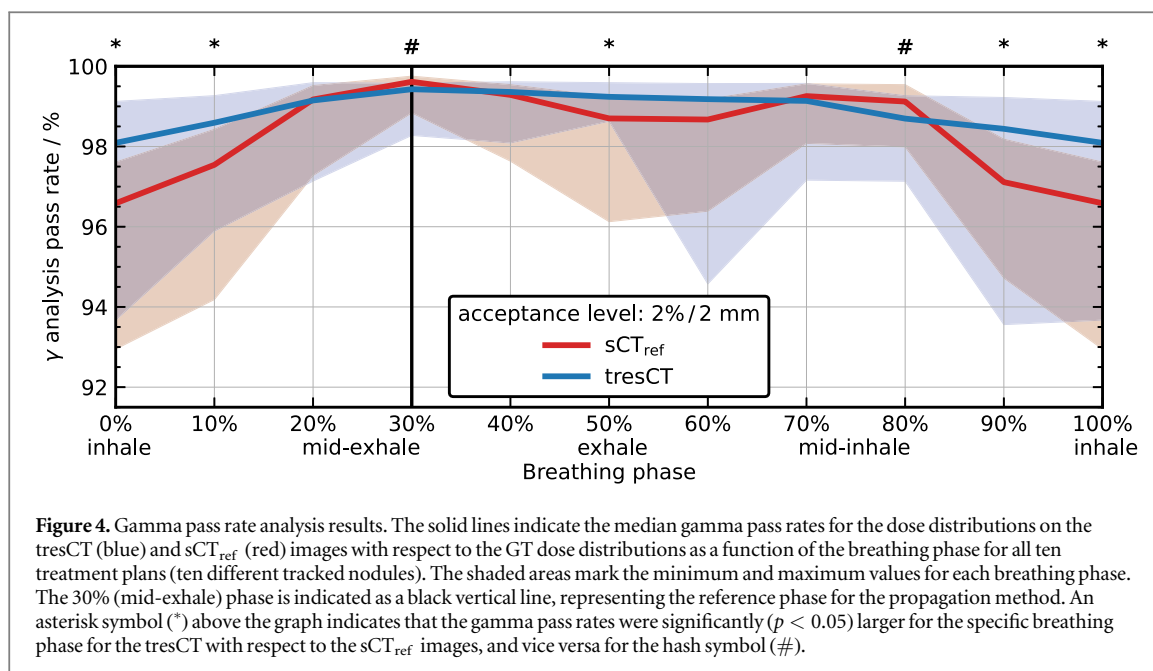
Exemplary sagittal views of GT and tresCT images (dataset 1 with orthogonal slices intersecting nodule 2) and their differences in the inhale and exhale phase at two different sagittal slice positions are depicted in figure 2. In these images, a high agreement between the GT and tresCT images can be observed for both the slice intersecting the GTV, as well as a distant slice in the contralateral lung. In general, slightly larger image differences were observed in the inhale than in the exhale phase.

### 3.2. Dose calculation evaluation

Figure 3 shows axial views of the GT and tresCT images and recalculated dose distributions for an exemplary dataset (dataset 3 with orthogonal slices intersecting nodule 3) and the respective relative dose differences for the inhale and exhale phase. For the majority of voxels in figure 3, the relative dose differences are positive (i.e. the dose is overestimated for the tresCT with respect to the GT image) for the inhale phase, and negative (i.e. the dose is underestimated for tresCT with respect to the GT image) for the exhale phase. For 54% (57%) of the voxels in the slice depicted in figure 3 with a dose level of at least 25% of  $D_p$ , the absolute dose difference was below 1%, and for 90% (95%) of the voxels the absolute dose difference was below 3% for the inhale (exhale) phase. The largest dose differences were observed in the high-dose region in the vicinity of the PTV boundary, with absolute dose differences of above 10%.







### 3.3. Gamma pass rate analysis

Figure 4 shows the gamma analysis results with a (2% of  $D_p/2$  mm) passing criterion as a function of the breathing phase for the tresCT and static sCT<sub>ref</sub> images. The median gamma pass rates were larger for the tresCT compared to the sCT<sub>ref</sub> images for all breathing phases except for the 20%, 30% (mid-exhale phase; breathing phase of the planning images and the reference images input to the propagation method), 70%, and 80% (mid-inhale phase) phases. In general, the more similar the images were to the mid-exhale phase image, the larger the median gamma pass rates were. Due to the asymmetric shape of the breathing curve, the anatomy in the exhale phase (50%) was more similar to the one in the mid-exhale phase (30%) than in the inhale phase (0%/100%), leading to the lowest median gamma pass rates for the latter for both the tresCT and the sCT<sub>ref</sub> images.

In the Wilcoxon signed rank tests, the tresCT images achieved significantly ( $p < 0.05$ ) larger gamma pass rates for the 0%, 10%, 50%, and 90% phases while the sCT<sub>ref</sub> achieved significantly ( $p < 0.05$ ) larger gamma pass rates for the 30% and 80% phases. No statistically significant differences ( $p > 0.05$ ) were found for the remaining breathing phases (20%, 40%, 60%, and 70%). Averaged over all breathing phases and datasets, the mean [min, max] gamma pass rates were 98.6% [93.6%, 99.6%] for the tresCT and 98.2% [92.6%, 99.8%] for the sCT<sub>ref</sub> images. The differences between tresCT and sCT<sub>ref</sub> for all breathing phases combined (tresCT with a 0.5% larger mean value than sCT<sub>ref</sub>) were statistically significant ( $p < 0.01$ ).

### 3.4. DVH parameter analysis

Figure 5 shows the cumulative DVHs for the GT, tresCT, and sCT<sub>ref</sub> images for dataset 2 where the orthogonal slices intersected nodule 2, for the GTV (nodule 2), nodules 1 and 3, and the lung for the inhale and exhale phase. For the exhale phase, the deviations of the cumulative DVHs of both the tresCT and sCT<sub>ref</sub> images with respect to the GT images were small for all analyzed structures. For the inhale phase, larger deviations for the GTV and the distant nodule 3 for sCT<sub>ref</sub> and for the GTV for tresCT with respect to the GT cumulative DVHs can be observed. No differences between the cumulative DVHs of the lung for the GT, tresCT, and sCT<sub>ref</sub> images are visible in figure 5 for neither the inhale nor the exhale phase.

The median absolute differences between the GT DVH parameters in the inhale and exhale phase, averaged over all ten datasets, were 4.1 Gy (7.4% relative difference) for the GTV  $D_{98\%}$ , 2.9 Gy (4.5%) for the GTV  $D_{50\%}$ , 1.7 Gy (2.5%) for the GTV  $D_{2\%}$ , 0.3 Gy (1.5%) for the nodules  $D_{50\%}$ , and 8.1 cc (2.0%) for the lung  $V_{20Gy}$ . Figure 6 shows  $\Delta_{\text{tresCT}}$  and  $\Delta_{\text{sCT}_{\text{ref}}}$  for all analyzed DVH parameters and datasets as a function of the breathing phase. In general, the median  $\Delta_{\text{tresCT}}$  and  $\Delta_{\text{sCT}_{\text{ref}}}$  values were largest (i.e. the largest deviations with respect to the GT values) for the breathing phases close to the inhale phase, followed by the exhale phase. The largest median  $\Delta_{\text{tresCT}}$  values were observed for the GTV  $D_{98\%}$  with a maximum value of 2.7% for the 0% phase. For the GTV  $D_{50\%}$ , GTV  $D_{2\%}$ , the nodules  $D_{50\%}$ , and the lung  $V_{20Gy}$  the median  $\Delta_{\text{tresCT}}$  was smaller than 2.3% for all breathing phases.

The breathing phase-specific Wilcoxon signed-rank test analysis indicated that  $\Delta_{\text{tresCT}}$  was significantly ( $p < 0.05$ ) smaller than  $\Delta_{\text{sCT}_{\text{ref}}}$  for the 0% and 10% phases for the GTV  $D_{98\%}$ , and for the 0%, 10%, and 90% phases for the GTV  $D_{50\%}$ .  $\Delta_{\text{sCT}_{\text{ref}}}$  was significantly ( $p < 0.05$ ) smaller than  $\Delta_{\text{tresCT}}$  only for the 30% phase for the

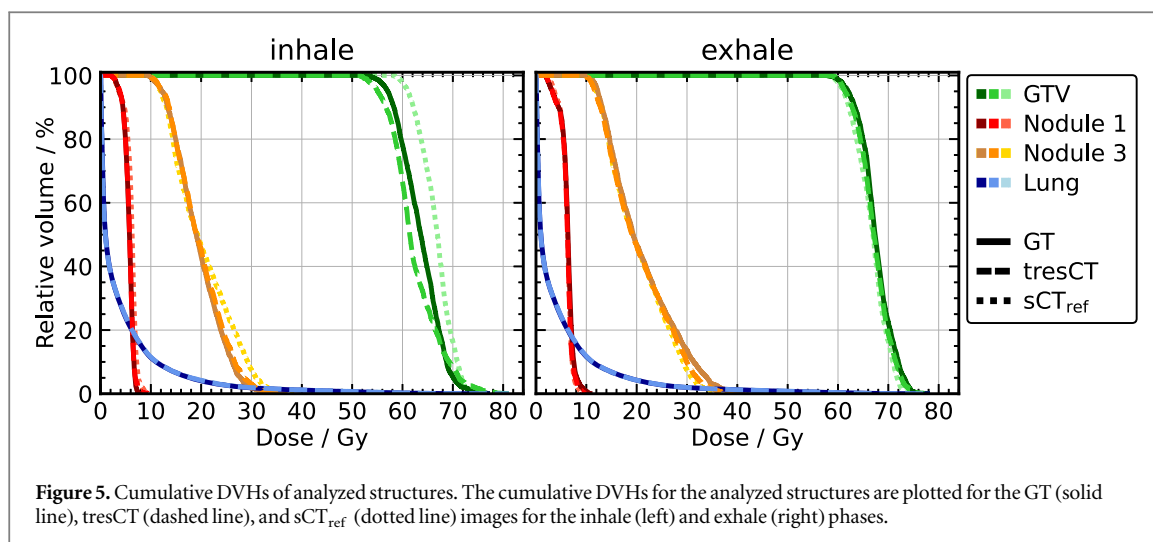


**Figure 5.** Cumulative DVHs of analyzed structures. The cumulative DVHs for the analyzed structures are plotted for the GT (solid line), tresCT (dashed line), and sCT<sub>ref</sub> (dotted line) images for the inhale (left) and exhale (right) phases.

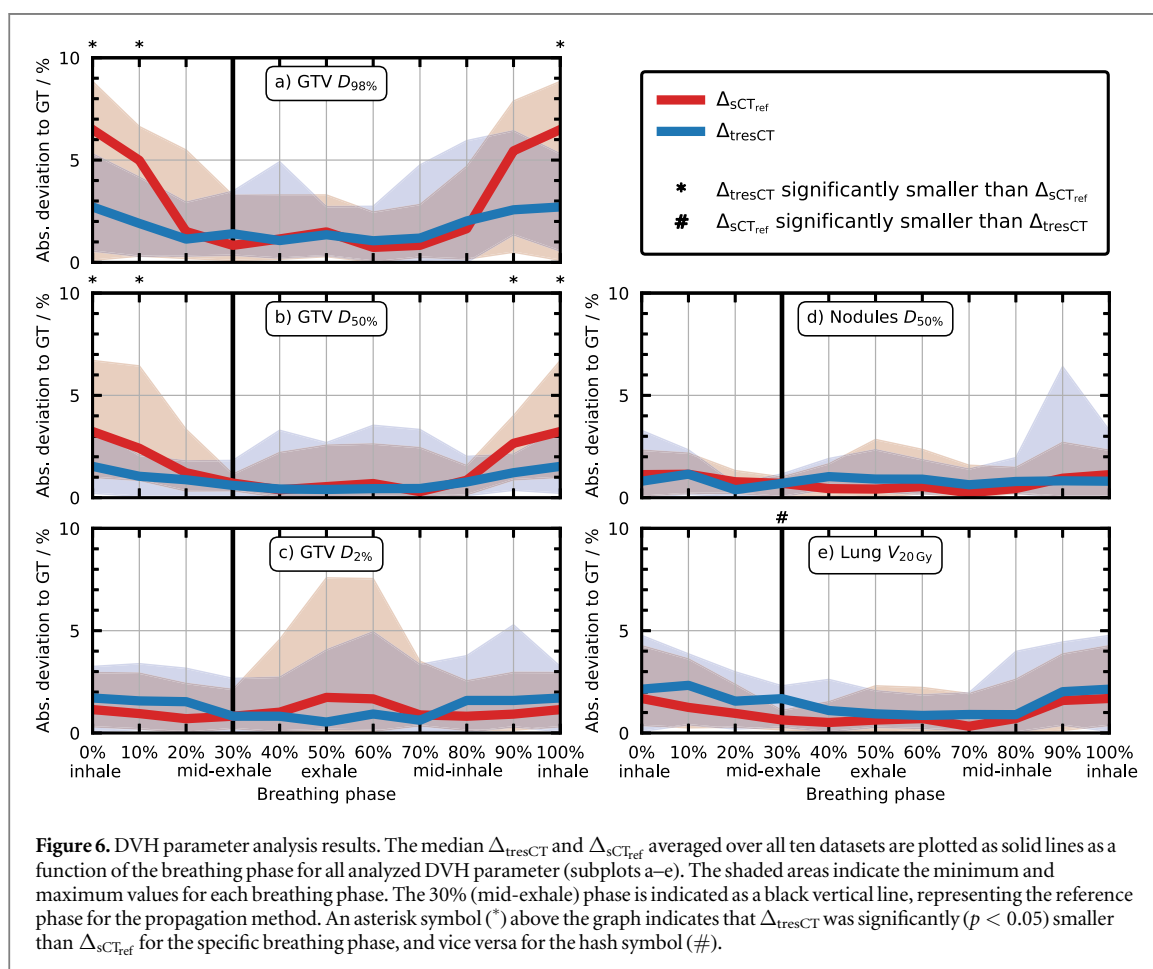


**Figure 6.** DVH parameter analysis results. The median  $\Delta_{\text{tresCT}}$  and  $\Delta_{\text{sCT}_{\text{ref}}}$  averaged over all ten datasets are plotted as solid lines as a function of the breathing phase for all analyzed DVH parameter (subplots a–e). The shaded areas indicate the minimum and maximum values for each breathing phase. The 30% (mid-exhale) phase is indicated as a black vertical line, representing the reference phase for the propagation method. An asterisk symbol (\*) above the graph indicates that  $\Delta_{\text{tresCT}}$  was significantly ( $p < 0.05$ ) smaller than  $\Delta_{\text{sCT}_{\text{ref}}}$  for the specific breathing phase, and vice versa for the hash symbol (#).

lung  $V_{20\text{Gy}}$ . No significant differences between  $\Delta_{\text{tresCT}}$  and  $\Delta_{\text{sCT}_{\text{ref}}}$  were observed for the GTV  $D_{2\%}$  and nodules  $D_{50\%}$ .

Averaged over all breathing phases and datasets, the median [5th percentile, 95th percentile] relative deviations of the tresCT with respect to the GT DVH parameters were +1.0% [−2.7%, +4.7%] for the GTV  $D_{98\%}$ , +0.4% [−1.9%, +1.9%] for the GTV  $D_{50\%}$ , +0.7% [−2.1%, +3.3%] for the GTV  $D_{2\%}$ , −0.5% [−1.9%, +1.6%] for the nodules  $D_{50\%}$ , and +1.1% [−0.9%, +3.9%] for the lung  $V_{20\text{Gy}}$ . The mean  $\Delta_{\text{tresCT}}$  and  $\Delta_{\text{sCT}_{\text{ref}}}$  values for all DVH parameters, averaged over all breathing phases and datasets are summarized in table 2. The mean  $\Delta_{\text{tresCT}}$  values were smaller by 25% and 40% compared to the  $\Delta_{\text{sCT}_{\text{ref}}}$  values for the GTV  $D_{98\%}$  and GTV  $D_{50\%}$ . The difference was statistically significant ( $p < 0.01$ ) for the GTV  $D_{50\%}$ . For the GTV  $D_{2\%}$  and nodules  $D_{50\%}$ , the mean  $\Delta_{\text{tresCT}}$  was slightly larger than the  $\Delta_{\text{sCT}_{\text{ref}}}$  value, but the difference was not statistically

**Table 2.** Mean absolute relative deviations of DVH parameters. The mean  $\Delta_{\text{tresCT}}$  and  $\Delta_{\text{sCT}_{\text{ref}}}$  values and their differences, averaged over all breathing phases and datasets are reported in %. The  $p$ -values of the Wilcoxon signed rank test are reported in the second to last column. An asterisk symbol (\*) indicates that the deviations were significantly ( $p < 0.05$ ) smaller for the the tresCT with respect to the sCT<sub>ref</sub> images, and vice versa for the hash symbol (#).

Parameter	$\Delta_{\text{sCT}_{\text{ref}}}$ %	$\Delta_{\text{tresCT}}$ %	$\Delta_{\text{tresCT}} - \Delta_{\text{sCT}_{\text{ref}}}$ %	$p$ -value	sig.
GTV $D_{98\%}$	2.4	1.9	-0.6	0.11	
GTV $D_{50\%}$	1.5	1.0	-0.6	<0.01	*
GTV $D_{2\%}$	1.3	1.4	+0.1	0.65	
Nodules $D_{50\%}$	0.8	1.0	+0.2	0.20	
Lung $V_{20\text{Gy}}$	1.1	1.5	+0.4	<0.01	#

significant ( $p > 0.05$ ). For the lung  $V_{20\text{Gy}}$ , the mean  $\Delta_{\text{tresCT}}$  (1.5%) was significantly ( $p < 0.01$ ) larger than the  $\Delta_{\text{sCT}_{\text{ref}}}$  (1.1%) value.

#### 4. Discussion

The presented tresCT generation method was based on previous work by Paganelli *et al* (2018b) and Rabe *et al* (2021). The propagation method was adapted and extended to additionally input a 3D-CT to output continuous tresCTs with a temporal resolution of 3.65 Hz and the voxel size of the acquired 4D-CT (voxel size:  $1.074 \times 1.074 \times 3 \text{ mm}^3$ ). The proposed method was experimentally validated with a porcine lung phantom by comparing the ten generated tresCTs to measured respiratory-correlated GT 4D-CT datasets in geometric and dose calculation analyses.

The geometrical analysis yielded a mean nodule motion amplitude of 8.2 mm. This is slightly larger than the 6 mm maximal motion that is allowed within a typically used gating window of 3 mm at the MRIdian MR-linac (van Sörnsen de Koste *et al* 2018, Regnery *et al* 2022). The average tracking error was smaller than the in-plane resolution of the cine MRI series images ( $3.5 \times 3.5 \text{ mm}^2$ ) for all nodules except for the nodule with the largest motion amplitude (dataset 2, nodule 3; motion amplitude: 15.9 mm; tracking error:  $(3.9 \pm 1.0) \text{ mm}$ ). Overall, the (mean  $\pm 1\sigma$ ) GTV tracking error averaged over all datasets and breathing phases was  $(2.1 \pm 0.8) \text{ mm}$ . This is slightly larger than the GTV tracking error reported by Rabe *et al* (2021) (median/95th percentile value of 1.5 mm/3.8 mm). The larger value found in the present study could be due to the fact that the GT and tresCT data were derived from imaging data acquired at two different scanners (CT scanner and MR-linac) instead of just the MRI scanner unit of the MRIdian, as in Rabe *et al* (2021). In agreement with the results described by Rabe *et al* (2021), the tracking error averaged over all breathing phases reported in this study tended to be larger for nodules with larger motion amplitudes (table 1).

A high agreement of the dose distributions calculated on the GT 4D-CT and randomly sampled tresCT images was found, with a median gamma pass rate of 98.6% with a (2% of  $D_p/2 \text{ mm}$ ) passing criterion. Overall, the accuracy of the tresCT DVH parameters was high for all breathing phases with a maximum median  $\Delta_{\text{tresCT}}$  value of 2.7% for the GTV  $D_{98\%}$  (inhale phase) and smaller than 2.3% for all other analyzed DVH parameters. The largest absolute relative deviations of up to  $\pm 10\%$  between the dose distributions were observed in the vicinity of the PTV margin in figure 3. In this area, the dose levels are high, the dose gradients are the steepest, and small geometric offsets of the GTV can lead to pronounced differences in the local dose distributions due to the large density differences of the lung tissue and gelatin nodule.

The gamma pass rate and DVH parameter accuracy of the tresCTs with respect to the GT datasets were breathing phase-dependent. The highest accuracy was achieved for images close to the breathing phase of the reference image used in the propagation method (mid-exhale phase). In general, the dose in the lung tissue surrounding the GTV was overestimated in the inhale phase, and underestimated in the exhale phase (figure 3). A possible explanation for this is that the applied lung density correction was not sufficiently accounting for the lung density changes within a breathing cycle.

Averaged over all datasets and breathing phases, the tresCTs significantly ( $p < 0.05$ ) outperformed the static sCT<sub>ref</sub> datasets in the dose calculation analyses for the gamma pass rate analysis (figure 4) and the DVH parameter GTV  $D_{50\%}$ . The mean  $\Delta_{\text{tresCT}}$  was smaller by 25% compared to the mean  $\Delta_{\text{sCT}_{\text{ref}}}$  for the GTV  $D_{98\%}$  and approximately the same for the GTV  $D_{2\%}$ , but these differences were not statistically significant ( $p > 0.05$ ). The results suggest that even for small motion amplitudes, like the residual motion within the gating window in breath-hold-gated treatments, the tresCTs can significantly improve the dose reconstruction accuracy to the GTV with respect to today's standard method where no motion and a static image (sCT<sub>ref</sub>) is assumed.

In contrast to patients, the porcine lung phantom allows the acquisition of GT datasets for validation of experimental methods, as previously demonstrated at the MRIdian system (Rabe *et al* 2021), and further imaging modalities (Meijers *et al* 2020, Schmitz *et al* 2021, Bondesson *et al* 2022). Therefore, the measurements presented in this study are an important step towards a potential clinical implementation but are subject to a few limitations. This includes properties of the phantom, such as the lack of a heart and lung perfusion, the fact that the lung motion is purely driven by an artificial silicon diaphragm without any chest movement, and the lower lung density compared to patients. For patients, a lower density difference between the lesions and the lung tissue is expected, which potentially results in smaller dose distribution perturbations due to the magnetic field in and close to the target compared to our results observed for the porcine lung. Furthermore, the geometric errors caused by potential slightly different motion patterns at the CT scanner and MR-linac could directly impact and bias the dose calculation results. By stabilizing the lung position with an uninterruptible power supply during transport, reproducible lung tumor motion at the CT scanner and MR-linac could be achieved. The high agreement between the tresCT and GT images and dose distributions suggest that these geometrical errors were small compared to the average nodule motion amplitudes.

Furthermore, the tresCT generation method is subject to the same limitations of the propagation method, as already identified and discussed by Paganelli *et al* (2018b) and Rabe *et al* (2021). Briefly summarized, this includes DIR uncertainties, the 3D DVF extrapolation, geometric distortions of the acquired orthogonal slices, the limited spatial resolution of the currently available cine MRI sequence, and the potential localization errors related to large out-of-plane motions. Additionally, the proposed tresCT generation method requires a synthetic 3D-CT image created with a DIR of a pre-treatment 3D-CT to a 3D-MRI. This workflow step introduces additional DIR uncertainties. To minimize these, the 3D-CT and 3D-MRI need to be acquired in a similar breathing phase. This was done accordingly in the presented experiments and is standard clinical practice at the MRIdian MR-linac today as part of the routine synthetic 3D-CT generation during treatment planning.

The tresCT generation method is intended to be applied during beam-on imaging at the MRIdian MR-linac. It only requires pre-treatment 3D-CT and 3D-MRI datasets and time-resolved orthogonal cine MRI series acquired during beam delivery as input data. The first clinically implemented version of the MRIdian MR-linac only allowed cine MRI acquisition for target motion monitoring and gated beam delivery of a single sagittal slice at 4 Hz (Klüter 2019) and in a later version at 8 Hz. The latest version (called the MRIdian A3i) now allows multi-planar target tracking with cine MRI acquisition of up to three orthogonal planes (Snyder *et al* 2023). Thus, all of the input data required for the tresCT generation method can already be acquired in clinical routine at the MRIdian A3i MR-linac today. Therefore, the method can potentially be clinically implemented with only a few minor changes to today's workflow.

While this study was focused on the ViewRay MRIdian MR-linac, the tresCT method could potentially also be employed at the 1.5 T Elekta Unity MR-linac (Winkel *et al* 2019). At the Unity MR-linac, orthogonal cine MRI can also be acquired during patient treatment (Jassar *et al* 2023), and intrafractional dose reconstruction based on imaging data acquired during patient treatment and linac log-file data has been demonstrated in the literature (Menten *et al* 2020).

For both the ViewRay MRIdian and the Elekta Unity MR-linac, one research goal is to develop real-time 3D cine MRI (also named real-time 4D-MRI) sequences that can be acquired during beam delivery (Paganelli *et al* 2018a, Stemkens *et al* 2018, Kurz *et al* 2020, Rabe *et al* 2020). Such a real-time 4D-MRI dataset could be used instead of the orthogonal cine MRI data used in the tresCT generation method to derive the DVFs to warp a reference synthetic 3D-CT to create time-resolved synthetic 4D-CT datasets (Johnstone *et al* 2018). Grimbergen *et al* recently reported on a reconstruction of the delivered dose at the Unity MR-linac based on a real-time 4D-MRI (Grimbergen *et al* 2023). However, these sequences cannot be easily adapted and employed at the MRIdian MR-linac with its low magnetic field strength of 0.35 T and restricted MRI hardware (Stemkens *et al* 2018, Klüter 2019). Therefore, the presented tresCT generation method might represent a valuable intermediate method for intrafractional reconstruction of the delivered dose for moving lung tumors until such sequences become potentially clinically available at the MRIdian MR-linac in the future.

## 5. Conclusions

We proposed a method to create continuous time-resolved estimated synthetic 4D-CTs (tresCTs) using 3D-CT, 3D-MRI, and orthogonal cine MRI series as input data. The method was experimentally validated with a porcine lung phantom. The resulting tresCTs achieved high agreement with measured GT respiratory-correlated 4D-CT datasets in terms of geometric and dose calculation accuracy. The proposed tresCT generation method could be a valuable tool for retrospective dose reconstruction or online intrafractional dose accumulation during MRgRT of lung cancer patients treated at the ViewRay MRIdian MR-linac. The simplicity of the method and the

similarity of the proposed workflow to today's clinical workflow could potentially enable a low-threshold clinical implementation in the future.

## Acknowledgments

This work was supported by the German Research Foundation (DFG) within the Research Training Group GRK 2274 'Advanced Medical Physics for Image-Guided Cancer Therapy'.

## Data availability statement

The data cannot be made publicly available upon publication because no suitable repository exists for hosting data in this field of study. The data that support the findings of this study are available upon reasonable request from the authors.

## Conflict of interest

The Department of Radiation Oncology of the University Hospital of LMU Munich has research agreements with Brainlab, Elekta and ViewRay.

## ORCID iDs

Moritz Rabe  <https://orcid.org/0000-0002-7085-4066>  
Henning Schmitz  <https://orcid.org/0000-0001-6143-1187>  
Giorgia Meschini  <https://orcid.org/0000-0001-8759-4291>  
Katia Parodi  <https://orcid.org/0000-0001-7779-6690>  
Guillaume Landry  <https://orcid.org/0000-0003-1707-4068>

## References

- Benedict S H *et al* 2010 Stereotactic body radiation therapy: the report of AAPM Task Group 101 *Med. Phys.* **37** 4078–101
- Biederer J and Heller M 2003 Artificial thorax for MR imaging studies in porcine heart-lung preparations *Radiology* **226** 250–5
- Bieri O and Scheffler K 2013 Fundamentals of balanced steady state free precession MRI *J. Magn. Reson. Imaging* **38** 2–11
- Bondesson D *et al* 2022 Anthropomorphic lung phantom based validation of in-room proton therapy 4D-CBCT image correction for dose calculation *Z. Med. Phys.* **32** 74–84
- Boye D, Lomax T and Knopf A 2013 Mapping motion from 4D-MRI to 3D-CT for use in 4D dose calculations: a technical feasibility study *Med. Phys.* **40** 061702
- Crockett C B *et al* 2021 Initial clinical experience of MR-guided radiotherapy for non-small cell lung cancer *Front. Oncol.* **11** 617681
- Finazzi T, de Koste J R V S, Palacios M A, Spoelstra F O, Slotman B J, Haasbeek C J and Senan S 2020c Delivery of magnetic resonance-guided single-fraction stereotactic lung radiotherapy *Phys. Imaging Radiat. Oncol.* **14** 17–23
- Finazzi T, Haasbeek C J, Spoelstra F O, Palacios M A, Admiraal M A, Bruynzeel A M, Slotman B J, Lagerwaard F J and Senan S 2020a Clinical outcomes of stereotactic MR-guided adaptive radiation therapy for high-risk lung tumors *Int. J. Radiat. Oncol. Biol. Phys.* **107** 270–8
- Finazzi T, Palacios M A, Haasbeek C J, Admiraal M A, Spoelstra F O, Bruynzeel A M, Slotman B J, Lagerwaard F J and Senan S 2020b Stereotactic MR-guided adaptive radiation therapy for peripheral lung tumors *Radiother. Oncol.* **144** 46–52
- Finazzi T, Palacios M A, Spoelstra F O, Haasbeek C J, Bruynzeel A M, Slotman B J, Lagerwaard F J and Senan S 2019 Role of on-table plan adaptation in MR-guided ablative radiation therapy for central lung tumors *Int. J. Radiat. Oncol. Biol. Phys.* **104** 933–41
- Freedman J N, Bainbridge H E, Nill S, Collins D J, Kachelrieß M, Leach M O, McDonald F, Oelfke U and Wetscherek A 2019 Synthetic 4D-CT of the thorax for treatment plan adaptation on MR-guided radiotherapy systems *Phys. Med. Biol.* **64** 115005
- Grimbergen G, Pötgens G G, Eijkelenkamp H, Raaymakers B W, Intven M P and Meijer G J 2023 Feasibility of delivered dose reconstruction for MR-guided SBRT of pancreatic tumors with fast, real-time 3D cine MRI *Radiother. Oncol.* **182** 109506
- Heath E, Unkelbach J and Oelfke U 2009 Incorporating uncertainties in respiratory motion into 4D treatment plan optimization *Med. Phys.* **36** 3059–71
- Henke L E *et al* 2019 Stereotactic MR-guided online adaptive radiation therapy (SMART) for ultracentral thorax malignancies: results of a phase 1 trial *Adv. Radiat. Oncol.* **4** 201–9
- Jassar H *et al* 2023 Real-time motion monitoring using orthogonal cine MRI during MR-guided adaptive radiation therapy for abdominal tumors on 1.5T MR-Linac *Med. Phys.* **50** 3103–16
- Johnstone E, Wyatt J J, Henry A M, Short S C, Sebag-Montefiore D, Murray L, Kelly C G, McCallum H M and Speight R 2018 Systematic review of synthetic computed tomography generation methodologies for use in magnetic resonance imaging-only radiation therapy *Int. J. Radiat. Oncol. Biol. Phys.* **100** 199–217
- Klüter S 2019 Technical design and concept of a 0.35 T MR-Linac *Clin. Transl. Radiat. Oncol.* **18** 98–101
- Kontaxis C, Bol G H, Legendijk J J W and Raaymakers B W 2015 A new methodology for inter- and intrafraction plan adaptation for the MR-linac *Phys. Med. Biol.* **60** 7485–97
- Kurz C *et al* 2020 Medical physics challenges in clinical MR-guided radiotherapy *Radiat. Oncol.* **15** 1–16
- Marx M, Ehrhardt J, Werner R, Schlemmer H-P and Handels H 2014 Simulation of spatiotemporal CT data sets using a 4D MRI-based lung motion model *Int. J. Comput. Assist. Radiol. Surg.* **9** 401–9

- McCarter S D and Beckham W A 2000 Evaluation of the validity of a convolution method for incorporating tumour movement and set-up variations into the radiotherapy treatment planning system *Phys. Med. Biol.* **45** 923–31
- McClelland J R, Hawkes D, Schaeffter T and King A 2013 Respiratory motion models: a review *Med. Image Anal.* **17** 19–42
- Meijers A et al 2020 Assessment of range uncertainty in lung-like tissue using a porcine lung phantom and proton radiography *Phys. Med. Biol.* **65** 155014
- Menten M J, Wetscherek A and Fast M F 2017 MRI-guided lung SBRT: present and future developments *Phys. Med.* **44** 139–49
- Menten M J et al 2020 Automatic reconstruction of the delivered dose of the day using MR-linac treatment log files and online MR imaging *Radiother. Oncol.* **145** 88–94
- Meschini G et al 2020 Virtual 4DCT from 4DMRI for the management of respiratory motion in carbon ion therapy of abdominal tumors *Med. Phys.* **47** 909–16
- Meschini G et al 2022 Time-resolved MRI for off-line treatment robustness evaluation in carbon-ion radiotherapy of pancreatic cancer *Med. Phys.* **49** 2386–95
- Müller M, Paganelli C and Keall P 2018 A phantom study to create synthetic CT from orthogonal two-dimensional cine MRI and evaluate the effect of irregular breathing *2018 40th Annual Int. Conf. of the IEEE Engineering in Medicine and Biology Society (EMBC)* 4162–5
- Nierer L et al 2022 Dosimetric benefit of MR-guided online adaptive radiotherapy in different tumor entities: liver, lung, abdominal lymph nodes, pancreas and prostate *Radiat. Oncol.* **17** 1–14
- Oh S A, Yea J W, Kim S K and Park J W 2019 Optimal gating window for respiratory-gated radiotherapy with real-time position management and respiration guiding system for liver cancer treatment *Sci. Rep.* **9** 1–6
- Paganelli C, Lee D, Kipritidis J, Whelan B, Greer P B, Baroni G, Riboldi M and Keall P 2018b Feasibility study on 3D image reconstruction from 2D orthogonal cine-MRI for MRI-guided radiotherapy *J. Med. Imaging Radiat. Oncol.* **62** 389–400
- Paganelli C, Portoso S, Garau N, Meschini G, Via R, Buizza G, Keall P, Riboldi M and Baroni G 2019 Time-resolved volumetric MRI in MRI-guided radiotherapy: an in silico comparative analysis *Phys. Med. Biol.* **64** 185013
- Paganelli C et al 2018a MRI-guidance for motion management in external beam radiotherapy: current status and future challenges *Phys. Med. Biol.* **63** 22TR03
- Palacios M A, Verheijen S, Schneiders F L, Bohoudi O, Slotman B J, Lagerwaard F J and Senan S 2022 Same-day consultation, simulation and lung stereotactic ablative radiotherapy delivery on a magnetic resonance-linac *Phys. Imaging Radiat. Oncol.* **24** 76–81
- Rabe M 2022 Investigation of time-resolved volumetric MRI to enhance MR-guided radiotherapy of moving lung tumors *PhD Thesis Ludwig-Maximilians-Universität München (LMU Munich), Munich, Germany* (<https://doi.org/10.5282/edoc.29244>)
- Rabe M, Palacios M A, van Sörnsen de Koste J R, Eze C, Hillbrand M, Belka C, Landry G, Senan S and Kurz C 2023 Comparison of MR-guided radiotherapy accumulated doses for central lung tumors with non-adaptive and online adaptive proton therapy *Med. Phys.* **50** 2625–36
- Rabe M et al 2020 Real-time 4DMRI-based internal target volume definition for moving lung tumors *Med. Phys.* **47** 1431–42
- Rabe M et al 2021 Porcine lung phantom-based validation of estimated 4D-MRI using orthogonal cine imaging for low-field MR-Linacs *Phys. Med. Biol.* **66** 055006
- Rao M, Wu J, Cao D, Wong T, Mehta V, Shepard D and Ye J 2012 Dosimetric impact of breathing motion in lung stereotactic body radiotherapy treatment using image-modulated radiotherapy and volumetric modulated arc therapy *Int. J. Radiat. Oncol. Biol. Phys.* **83** e251–6
- Regnery S et al 2022 Adaptive MR-guided stereotactic radiotherapy is beneficial for ablative treatment of lung tumors in high-risk locations *Front. Oncol.* **11** 1–10
- Regnery S et al 2023 To fly or not to fly: stereotactic MR-guided adaptive radiotherapy effectively treats ultracentral lung tumors with favorable long-term outcomes *Lung Cancer* **179** 107175
- Sarrut D, Boldea V, Miguet S and Ginestet C 2006 Simulation of four-dimensional CT images from deformable registration between inhale and exhale breath-hold CT scans *Med. Phys.* **33** 605–17
- Schmitz H et al 2021 Validation of proton dose calculation on scatter corrected 4D cone beam computed tomography using a porcine lung phantom *Phys. Med. Biol.* **66** 175022
- Shackelford J A, Kandasamy N and Sharp G C 2010 On developing B-spline registration algorithms for multi-core processors *Phys. Med. Biol.* **55** 6329–51
- Sharma M, Weiss E and Siebers J V 2012 Dose deformation-invariance in adaptive prostate radiation therapy: implication for treatment simulations *Radiother. Oncol.* **105** 207–13
- Snyder K C, Mao W, Kim J P, Cunningham J, Chetty I J, Siddiqui S M, Parikh P and Dolan J 2023 Commissioning, clinical implementation, and initial experience with a new brain tumor treatment package on a low-field MR-linac *J. Appl. Clin. Med. Phys.* **24** e13919
- Stemkens B, Paulson E S and Tijssen R H N 2018 Nuts and bolts of 4D-MRI for radiotherapy *Phys. Med. Biol.* **63** 21TR01
- van Herk M, McWilliam A, Dubec M, Faivre-Finn C and Choudhury A 2018 Magnetic resonance imaging-guided radiation therapy: a short strengths, weaknesses, opportunities, and threats analysis *Int. J. Radiat. Oncol. Biol. Phys.* **101** 1057–60
- van Sörnsen de Koste J R, Palacios M A, Bruynzeel A M, Slotman B J, Senan S and Lagerwaard F J 2018 MR-guided gated stereotactic radiation therapy delivery for lung, adrenal, and pancreatic tumors: a geometric analysis *Int. J. Radiat. Oncol. Biol. Phys.* **102** 858–66
- von Münchow A et al 2022 Statistical breathing curve sampling to quantify interplay effects of moving lung tumors in a 4D Monte Carlo dose calculation framework *Phys. Med.* **101** 104–11
- Wahlstedt I et al 2022 Gating has a negligible impact on dose delivered in MRI-guided online adaptive radiotherapy of prostate cancer *Radiother. Oncol.* **170** 205–12
- Wahlstedt I et al 2023 Interfractional dose accumulation for MR-guided liver SBRT: variation among algorithms is highly patient- and fraction-dependent *Radiother. Oncol.* **182** 109448
- Winkel D et al 2019 Adaptive radiotherapy: the Elekta Unity MR-linac concept *Clin. Transl. Radiat. Oncol.* **18** 54–9
- Xiong Y, Rabe M, Nierer L, Kawula M, Corradini S, Belka C, Riboldi M, Landry G and Kurz C 2022 Assessment of intrafractional prostate motion and its dosimetric impact in MRI-guided online adaptive radiotherapy with gating *Strahlenther. Onkol.* **199** 544–53
- Yang Y X, Teo S-K, Van Reeth E, Tan C H, Tham I W K and Poh C L 2015 A hybrid approach for fusing 4D-MRI temporal information with 3D-CT for the study of lung and lung tumor motion *Med. Phys.* **42** 4484–96